Aerospace Science and Technology 137 (2023) 108281

Contents lists available at ScienceDirect

Aerospace Science and Technology

journal homepage: www.elsevier.com/locate/aescte

# Numerical analysis of combustion noise in an atmospheric swirl-stabilized LDI burner through modal decomposition techniques

A. Broatch, M. Carreres, J. García-Tíscar *, M. Rodríguez-Pastor

*CMT – Motores Térmicos, Universitat Politècnica de València, Camino de Vera, 46022 Valencia, Spain*

ARTICLE INFO

*Article history:*
Received 14 September 2022
Received in revised form 13 January 2023
Accepted 22 March 2023
Available online 28 March 2023
Communicated by Suresh Menon

*Keywords:*
Combustion noise
Lean Direct Injection
Proper Orthogonal Decomposition
Dynamic Mode Decomposition
Precessing Vortex Core

ABSTRACT

Combustion noise in gas turbine engines has recently become a relevant source of noise in the aircraft due to the appearance of new burner architectures that are intrinsically more unstable, and the optimization of other conventional noise sources in this mean of transport (e.g., jet, fan, airframe). In this work, a simulation setup for reactive conditions was prepared in the CONVERGE finite-volume package using the detailed chemistry SAGE solver to model the combustion of a benchmark case, which was solved using a LES approach with three different cell base sizes: 8,10,12 mm. A confined liquid-fueled swirl-stabilized burner located at the CORIA Laboratory, France, was used to validate the numerical results with the experimental measurements obtained at this facility. OH-PLIF measurements and PDA results for both phases were used to guarantee the accuracy of the numerical OH contours and the velocity profiles of both phases. These experimental measurements were collected at CORIA. After ensuring the stabilization of the numerical flame, the reactive simulations were extended with some adjustments in the time step to capture the acoustic motion. Several techniques like Fast Fourier Transform (FFT), Proper Orthogonal Decomposition (POD) and Dynamic Mode Decomposition (DMD) were used to analyze these results and confirm the presence of a Precessing Vortex Core (PVC) and a Vortex Breakdown Bubble (VBB) during the coupling of pressure, axial velocity and fuel mass fraction in reactive conditions. Furthermore, the acoustic analysis performed with a Helmholtz solver proved that the second longitudinal mode of the chamber (310 Hz) was present in the pressure signal (300 Hz in the LES calculations) and resonated with the Vortex Breakdown Bubble (VBB). However, this dominant frequency did not appear in the frequency distribution of the OH mass fraction and no feedback interaction between the acoustic and the combustion happened. Thus, only combustion noise was obtained.



## 1. Introduction

Lean Direct Injection engines have become one of the most promising technologies for liquid-fueled combustors to reduce NOx emissions in the next generation of gas turbines [1]. In this type of architecture, fuel is directly injected in the combustion chamber, where the atomization, evaporation and mixing processes take place. A swirler promotes all these phenomena and helps obtaining a lean and uniform mixture fraction distribution that avoids the generation of the previously mentioned radicals through the thermal mechanism. Furthermore, it also works as an aerodynamic flame holder in reactive conditions [2]. However, one of its main drawbacks is the appearance of combustion instabilities and noise for some operating conditions [3].

These phenomena are unsteady and related with the perturbations of the relevant fields of the system (e.g., flame surface, mixture fraction, pressure). For this reason, fully-compressible Large-Eddy Simulation (LES) formulations have become one of the best options to look into them [4]. The formulation of the equations already includes the resolution of the acoustic part of the perturbations, while the largest turbulent scales in the system are also solved according to the chosen grid scale. The smallest turbulent scales remain unresolved and can be modeled through a sub-grid model.

However, the numerical resolution of turbulent spray-flames in reactive conditions still has some issues that must be assessed for properly performing the computations. First, gaseous and liquid phases must be computed in the correct framework. Eulerian – Eulerian [5] and Eulerian – Lagrangian [6] are some of the approximations used in the bibliography to deal with both phases respectively. The most common one is the Eulerian – Lagrangian, solving the gaseous phase with a traditional Eulerian approximation while tracking the droplets with the Lagrangian framework.

* Corresponding author.
*E-mail address:* jorgarti@mot.upv.es (J. García-Tíscar).

https://doi.org/10.1016/j.ast.2023.108281

Second, a proper resolution at the flame front must be achieved to correctly capture the fluctuations of the flame front. Laminar flame thickness is usually in the order of hundreds of microns for this kind of applications [7]. Flame front is ideally discretized in five elements [8], so the computational cost of these simulations can become very demanding. For this reason, alternative combustion models like the Dynamic Thickened Flame [9] appeared to artificially increase the flame thickness and reduce the size of the required mesh. However, the effect that this lack of resolution has in the prediction of direct combustion noise for confined swirl-stabilized spray-flame burners requires further research.

This paper analyzes the phenomena that lead to the generation of combustion noise in the CORIA Spray LDI burner under stable operating conditions using decomposition techniques. Furthermore, the effects of grid resolution on the combustion parameters and the generated noise are checked through three different LES (minimum base cell size of 0.25, 0.3125, 0.375 mm respectively). A complete CFD model using a Eulerian-Lagrangian framework and a detailed chemistry solver was setup in the finite-volume solver CONVERGE. The results of the reactive simulations were validated with the experimental results measured at CORIA: experimental velocity profiles obtained for both phases at different axial stations of the burner and the OH contours got from OH-PLIF tests. After validating the numerical results and ensuring the stabilization of the flame, the acoustic simulations were computed with the corresponding time step adjustments.

These results were analyzed with point-based FFT techniques and complex 3D Reduction Order Models (i.e., Proper Orthogonal Decomposition (POD) and Dynamic Mode Decomposition (DMD)). These models have proved to be a reliable way to simplify complex phenomena and understand the effects of acoustic and hydrodynamic modes [10,11]. These algorithms also provide information about the interactions between the spray, the acoustics and the flame, one of the largest issues in this kind of combustors [12]. Particularly, DMD is a robust tool to understand the couplings between the most relevant variables in LDI engines [13]. However, the decompositions must be performed in the whole chamber domain to obtain accurate representations of the acoustic modes, increasing notoriously the computational cost [13].

For this reason, a Helmholtz solver has been used to complement the analysis. LES computations are very useful to obtain detailed information about the variables involved in the phenomena and how they interact with each other, but they do not explain the nature of the dominant frequencies if another model is not used [14,15]. These solvers can help identifying the presence of acoustic modes.

Both analysis tools were used to confirm the presence of hydrodynamic modes that affect the system (i.e., Precessing Vortex Core [16] and Vortex Breakdown Bubble) during the combustion, while one of the acoustic longitudinal modes was excited too.

## 2. Case setup and postprocessing techniques

### 2.1. Experimental combustor description

The chosen benchmark case was a confined atmospheric burner set up at the CORIA laboratory (CORIA Spray LDI burner). This facility is conformed by a combustion chamber, an exhaust nozzle and a plenum to uniformize the flow before getting into the chamber. The dimensions of the chamber are 100 × 100 × 260 mm and a radial swirler of 18 vanes with an angle of 45 º is disposed at the inlet of the chamber to help the evaporation and mixture process of the fuel (n-heptane in this case.). More information about the experimental results used in this paper to validate the simulations can be found in [17,18]. In reactive conditions, experimental velocity profiles for both phases at different axial stations and OH contours were used. The initial aim of these experimental campaigns was to characterize the velocity distribution and properties for both phases, providing also useful experimental data that helped to explain and model numerically the ignition mechanisms in aeronautical spray burners [19,20]. However, pressure signals were recorded during the ignition sequences with a transducer positioned at the exhaust nozzle. In this paper, these signals recorded at 10 kHz were used to validate the direct noise computed using the fully compressible LES solver.

The work done in this paper was a continuation of the analysis performed in [21,22] for the non-reactive case, so the same operating condition was adopted ($T_{air} = 416$ K, $\dot{m}_{fuel} = 0.33$ g/s, $\dot{m}_{air} = 8.2$ g/s, $\Phi = 0.61$).

### 2.2. General equations and submodels

#### 2.2.1. Governing equations

Compressible transport equations were used in the CFD calculations. The momentum and mass equations were:

$$\frac{\partial \rho}{\partial t} + \nabla \cdot (\rho \bar{u}) = \dot{S}_\rho \tag{1}$$

$$\frac{\partial \rho \bar{u}}{\partial t} + \nabla \cdot (\rho \bar{u} \otimes \bar{u}) = -\nabla P + \nabla \cdot \bar{\sigma} + \dot{S}_M \tag{2}$$

where the viscous stress tensor ($\bar{\sigma}$) was:

$$\bar{\sigma} = \mu(\nabla \otimes \bar{u} + \nabla \otimes \bar{u}^T) - \frac{2}{3}\mu(\nabla \cdot \bar{u})I \tag{3}$$

Source terms in both equations ($\dot{\rho}$, $\dot{S}_M$) were related to the evaporation, the appearance of combustion products and the coupling of the spray. The transport equation of energy could be expressed as:

$$\frac{\partial \rho e}{\partial t} + \nabla \cdot (\rho \bar{u} e) = -\nabla \cdot (P\bar{u}) + \nabla \cdot (\bar{u}\sigma) + \nabla \cdot J + \nabla \cdot \left(\frac{K_t}{C_v} \nabla e\right) + \dot{Q}_S \tag{4}$$

where the energy transport due to the species diffusion ($J$) was:

$$J = \left(\sum_j h_j \rho D_t - \sum_j e_j \gamma \frac{K}{C_p}\right) \nabla Y_j \tag{5}$$

Contribution of each species to the specific enthalpy, internal energy and mass fraction ($h_j$, $e_j$, $Y_j$) was considered. The conservation of mass associated with each species could be generally expressed as:

$$\frac{\partial \rho_j}{\partial t} + \nabla \cdot (\rho_j \bar{u}) = \nabla \cdot (\rho D_t \nabla Y_j) + \dot{\omega}_j \tag{6}$$

Ideal gas law was used in these CFD simulations as the equation of state. Turbulent conductivity ($K_t$) in Eqn. (4) and turbulent mass diffusion coefficient $D_t$ in Eqn. (5), (6) could be expressed as:

$$K_t = K + C_p \frac{\mu_t}{Pr_t} \tag{7}$$

$$D_t = \frac{\nu_t}{Sc_t} \tag{8}$$

Both expressions depend on the turbulent Prandtl and Schmidt ($Pr_t$, $Sc_t$) beyond the turbulent viscosity ($\mu_t$, $\nu_t$). Their values were set to 0.7 in these calculations.

Regarding the governing equations of the liquid phase, the formulation used here was identical to the one in [21]. Readers are referred to that paper to know more details about the Lagrangian formulation used.

*2.2.2. Turbulent combustion model*

A detailed chemistry solver called SAGE [23] was used in these simulations. The details of this solver have been extensively described in the bibliography, so only a summary of the main characteristics has been reviewed in this section. Readers are referred to [23,24] to find more details about this model. SAGE solver uses the principles of chemical kinetics to compute all the reaction rates of the chosen mechanism at each cell of the domain every timestep. In this way, the source term related to the generation of every species ($\dot{\omega}_j$ in Eqn. (6)) is computed before the transport equations, providing these data to the PISO algorithm. Thus, SAGE solver needed a mechanism file with all the elementary reactions to obtain an accurate solution for the species. These reactions were expressed in the modified Arrhenius format, whose forward reaction rate was given by the expression:

$$k_{i,f} = A_i T^{\beta_i} \exp\left(\frac{-E_i}{RT}\right) \tag{9}$$

where $A_i$ is the pre-exponential factor, $\beta_i$ is the temperature exponent, $E_i$ is the activation energy and $R$ is the ideal gas constant of the reaction $i$. Reverse reaction rates were computed from the properties in a thermodynamic data file generated for n-heptane in CONVERGE.

Mechanism choice was a fundamental part to obtain reliable results with respect to the combustion phenomena. However, computational cost became unaffordable for large mechanisms due to the time required to solve all the reaction rates for each elementary reaction. In this way, a Small Skeletal Mechanism with 28 species and 57 reactions created through the ACR method in [25] was used in this paper. This mechanism was optimized to recreate properly the flame propagation and the laminar flame speed.

*2.2.3. Closure equations*

Regarding the turbulence model, the Dynamic Smagorinsky LES sub-grid model [26] was used due to the accuracy that it showed for the most refined cases in other studies performed on this combustor [21,27]. The sub-grid interactions between the chemistry and the turbulence were not modeled.

*2.2.4. Spray submodels*

All the spray submodels were nearly identical to the ones explained in [21], so only the most important differences will be presented here. TAB model [28] was adopted to deal with the atomization and breakup as it showed the best agreement with respect to the experimental measurements in the aforementioned study. In this case, the spray was a hollow-cone type with an external angle of 80º and a thickness of 8º, the droplet size distribution was a Rosin-Rammler with a Sauter Mean Diameter ($D_{32}$) of 31 µm and a width parameter ($q$) of 2.3.

An Eulerian-Lagrangian approach was used to track the droplets as parcels along the domain. These parcels gather droplets with similar thermodynamic properties (e.g., temperature, mass, velocity). A larger amount of parcels were used in this work ($25 \cdot 10^6$ parcels/s) with respect the non-reactive paper ($3 \cdot 10^6$ parcels/s) to preserve the amount of liquid per cell and avoid artificial distortions of the droplet drag with respect to the additional level of refinement used in this case.

*2.3. Mesh strategy*

A regular mesh made of orthogonal hexahedrons was used for the CFD computations. This software uses a sophisticated meshing technique where a cartesian grid is elaborated in first instance. Then, the grid is cut according to the geometry. Cells that intersect with the surface may have arbitrary-sided polyhedra and can merge with the adjacent elements if their volume is lower than a certain threshold. Additional meshing techniques (e.g., fixed embedding or Automated Mesh Refinement) were referenced from the base size depending on the level of desired refinement, being $L_{res} = L_{base}/2^{level}$. In these simulations, an atmospheric reservoir was appended at the outlet of the nozzle to avoid setting an unknown acoustic boundary condition there. Base size was defined as a trade-off between the dissipation of the acoustic waves in the reservoir and the maximum refinement levels that CONVERGE can apply to obtain a suitable flame resolution (5-6 levels). Thus, the base size of the 3 LES performed on this sensitivity study was 8,10 and 12 mm.

Fixed embedding was widely used in the setup of these cases, a refinement of 2 levels on all the plenum and the combustion chamber were applied to obtain a good resolution of the flow and adequate LES quality parameters. Furthermore, 5 levels of refinement were used in the injection cone angle and the swirler to obtain a well-resolved flow in the injection plane and the lift-off region.

Regarding the Automated Mesh refinement, this grid control strategy was activated for the velocity and the temperature to obtain a fine resolution at the flame front regardless of its position. Five levels of refinement were used for both variables. The sub-grid threshold values that activated the AMR refinement were $T_{sgs} = 3.8$ K, $v_{sgs} = 1.5$ m/s and $N_{parcels} = 80$. The mesh size was limited to 20 million cells, but it was not achieved in any of the calculated simulations. Werner and Wengle law [29] was used in this case for the near-wall treatment. Boundary layer refinement at the plenum and the combustion chamber was defined using two layers of 3 levels of fixed embedding refinement.

The resultant meshes had an average size of 7, 9.5, 15 M respectively. A scheme of the CORIA Spray LDI burner and all the strategies used for grid control can be observed in Fig. 1.

*2.4. Numerical approach*

Regarding the solver in the CFD calculations, equations related to the gas were solved in the compressible form, while the liquid was assumed to be in the incompressible regime. The propagation of the transport equations was done using a version of the PISO algorithm implemented in this software [30].

Regarding the combustion, computational cost would have been unaffordable if the solution of the ODEs had to be calculated for each cell of the domain. For this reason, a threshold temperature was defined to prescribe the presence of reactivity (600 K), while the adaptive zoning for temperature and reaction rate was used to compute the reaction rates of the species in bins of cells.

Time step was controlled using the CFL criteria. Convective ($u\frac{\Delta t}{\Delta x}$) and Mach ($c\frac{\Delta t}{\Delta x}$) numbers were modified during the simulations and restricted consequently the value of the increment of time per iteration. During non-reactive and combustion simulations, the aforementioned criteria were set to 1 and 50 respectively, the first one being the most restrictive value. A common time step was between $1.5 - 2.5 \cdot 10^{-6}$ s for the finest case. CFL criteria had to be adjusted in order to properly capture the propagation of the acoustic waves during acoustic simulations. For this reason, the Mach criterion was set to 1 during the last part of the numerical campaign. The resultant time steps were $1 - 2 \cdot 10^{-7}$ s for the case with a base size of 8 mm.

*2.5. Simulation time-schedule strategy and boundary conditions*

First, a gaseous simulation was calculated to initialize the velocity fields of the system and stabilize the coherent structures of the flow before the start of the injection. Base size was 12 mm in this simulation and no AMR was used, the whole grid was scaled

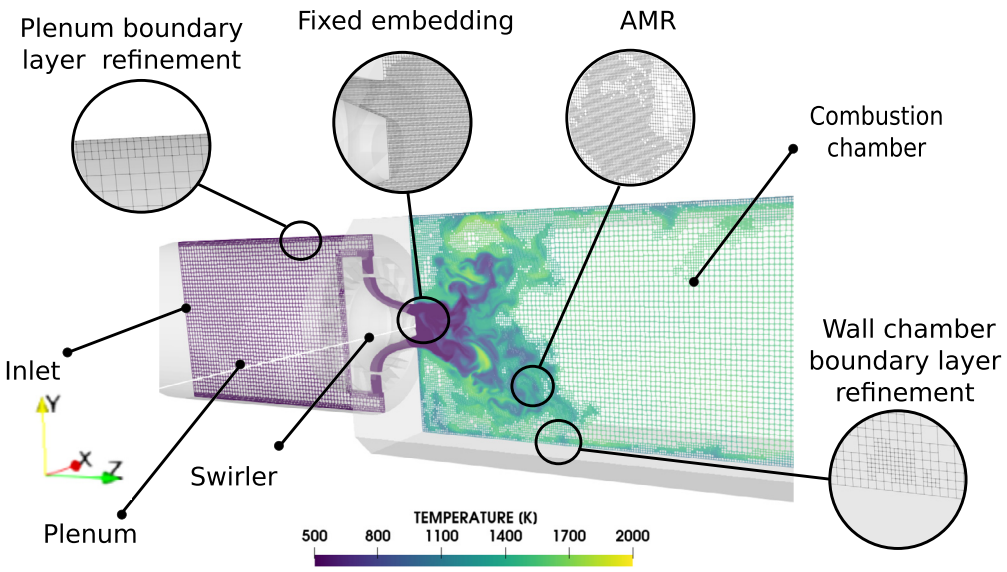


**Fig. 1.** Scheme of the CORIA Spray LDI burner with all the fixed embedding, AMR regions and boundary layer refinements used. Simulated operating conditions were $\dot{m}_{air} = 8.2$ g/s, $\dot{m}_{fuel} = 0.33$ g/s, $T_{air} = 416$ K and $T_{fuel} = 350$ K.

to $2^{-1}$ the first 50 ms to speed up the calculations. Injection cone refinement began just before the first drops came into the chamber (145 ms).

Then, the non-reactive simulation was launched from a map of the main variables obtained from the gaseous calculation. AMR was activated and the sub-grid adjustments were set like in [21] except for the base size, which was larger (12 mm). This size was defined to reduce the computational time required to obtain a rich enough equivalence ratio field to ignite the system.

Combustion began at 470 ms with the map obtained at the end of the non-reactive simulation. A new base size and fixed embedding refinements were defined according to the information provided in Sec. 2.3. Ignition was provoked using a sphere of energy with center in [0,0.04,0.03] m and a radius of 0.01 m. The energy applied was 100 J and the maximum temperature that it could achieve was clipped to 2000 K, the source was activated during 3 ms (472-475 ms). All the fixed embeddings were applied from the beginning and a general coarsening of the mesh was applied again using the grid scale from 470 ms to 600 ms in order to stabilize the conditions in the chamber (e.g., overall equivalence ratio, global heat release, maximum temperature). After that, the grid scale was removed and the AMR was activated. The reactive flow had 25 ms to get used to the final mesh strategy. Mean and RMS results were averaged for the next 100 ms before the acoustic simulation. Finally, acoustic cases were calculated after ensuring the convergence and the stabilization of the flame during the next 20 ms. An overview of the strategy followed in the simulations can be observed in Fig. 2. The computational cost of the reactive and thermoacoustic simulations for the three meshes can be found in Table A.1 of the Appendix.

Surfaces were gathered in different groups depending on the type of boundary condition that was applied. These groups can be observed in Fig. 3. In this way, an inlet condition with $\dot{m}_{air} = 8.2$ g/s and $T_{air} = 416$ K was defined at the inlet surface of the plenum. Plenum and swirler walls had a no-slip velocity condition associated, the temperature was set at 387 K for both flow conditions. Chamber walls in reactive regime had identical boundary conditions but their temperature was 1000 K to enhance the evaporation of the droplets. This condition was already used in other simulations of this combustor with reasonable results [20]. Regarding the reservoir boundary conditions, atmospheric pressure was prescribed at the outlet, while the velocity profile was

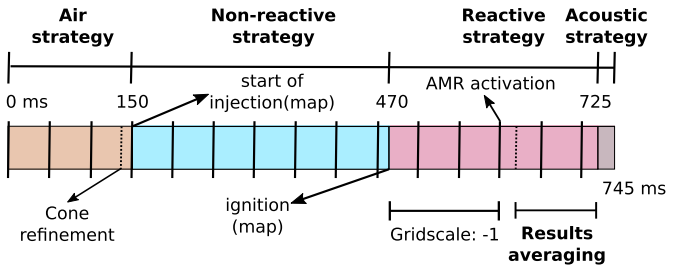


**Fig. 2.** Time-schedule and strategy followed in the simulations of the CORIA Spray LDI burner.

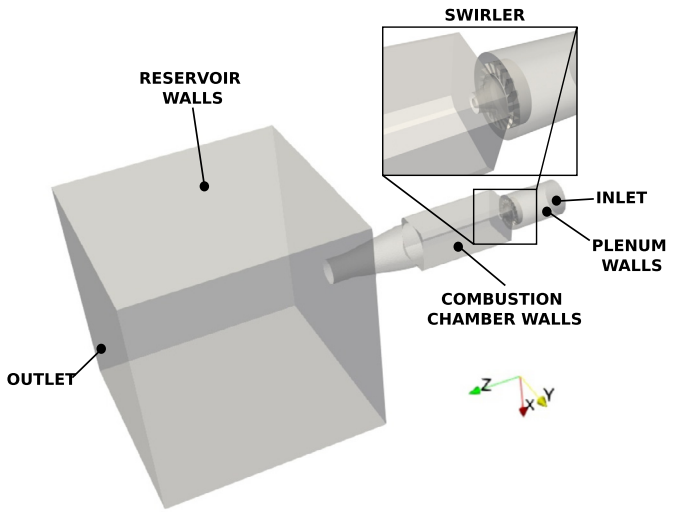


**Fig. 3.** Computational domain and boundary conditions used for the simulations of the CORIA Spray LDI burner.

assumed to be fully developed using a zero-normal velocity gradient for both flow regimes (non-reactive and combustion). The rest of the reservoir surfaces were assumed to behave like a wall for non-reactive flow, while they were changed to the aforementioned outlet condition during the combustion simulations due to the expected expansion of the exhaust jet.

### 2.6. Modal decomposition techniques

As explained in the introduction, modal decomposition techniques have proven to be a reliable method to extract relevant dynamic data from complex flow that involve multifactorial phenomena. The methodology followed to perform Proper Orthogonal Decomposition (POD) and Dynamic Mode Decomposition (DMD) from the 3D snapshots collected during the thermoacoustic simulations was identical to the one in [22,31].

The analysis was performed from 400 snapshots computed during 20 ms with a sampling frequency of 20 kHz (constant $\Delta t$ of 0.05 ms between the snapshots). The variables used for the decomposition were the fuel mass fraction ($Y_{C_7H_{16}}$), the mass fraction of OH ($Y_{OH}$), the instantaneous axial velocity (W) and pressure (P). These magnitudes were chosen due to their relevance on the combustion, the hydrodynamics and the acoustics of the system.

#### 2.6.1. Data preconditioning

The implementation of both algorithms in this case were based on the Singular Value Decomposition (SVD) of an input matrix that represents the temporal evolution of a variable of interest related to the flowfield. This algorithm is a matrix factorization that tries to generalize the eigendecomposition for a rectangular matrix [32]. The general expression for this decomposition is:

$$V = U \Sigma W^T \tag{10}$$

Where U and W are related to the left and right singular eigenvectors, which are stored on the columns of each matrix respectively. The number of rows of these matrices is determined by the number of cells in the included domain ($M$), while the number of columns is equal to the number of snapshots ($N$). $\Sigma$ represents a diagonal matrix where its terms are already ordered according to their magnitude, so $\sigma_1 \geq \sigma_2 \geq \ldots \geq \sigma_N$. The interpretation of these matrices changes according to the postprocessing technique, so it will be explained on the particular subsections of POD and DMD.

A matrix that expresses the temporal evolution of the flowfield must be gathered before applying the SVD decomposition ($V$). This matrix can be represented as:

$$V = [\bar{v}_1, \bar{v}_2, \ldots, \bar{v}_N] \tag{11}$$

Where $\bar{v}_N$ is the column vector of the $N$ snapshot that contains the information of the spatial flowfield. However, the AMR generated a mesh that varied on each instant of time, so an additional processing of the data was required to interpolate the data to a static mesh that could provide a coherent $V$ matrix.

First, a set of one million cells was randomly chosen in the combustion chamber for the instant of time with the most refined mesh. This number of cells was determined in previous works to be enough to determine the dynamics of the flowfield without having a large computational cost. Then, the cells that were closest to the centroids of the reference mesh were identified for all the instants of time. If the euclidean distance between the reference centroid and the new one was lower than 1 mm, the new values were assigned to the reference centroid. If not, a "NaN" was listed for the cell value in the vector column related to that instant of time. Finally, the rows of the V matrix that contained "NaN" values or whose centroid position was larger than an axial threshold (60 mm in this case) were removed from the matrix. In this way, a compact matrix with non-infinite terms related to centroids where the most relevant dynamic phenomena take place could be generated.

After this, the possibility of removing the temporal mean of the snapshots on each cell was assessed. On one hand, POD tries to find a deterministic function that best approximates a zero-mean stochastic process [33]. The snapshots gathered in the V matrix were considered as random realizations of the phenomena and the POD modeled these fluctuations. Thus, the temporal average of the V matrix had to be removed before applying the POD technique.

On the other hand, DMD does not necessarily require to remove the temporal mean [34]. However, Towne et al. [33] remarked that performing the DMD on zero-mean matrices in stationary flows could be useful to mimic the zero-growth rate property of the Koopman modes. In the end, DMD tries to offer an approximate solution of this linear operator, so it could be interesting to consider it in this statistically stationary flow.

It was observed that the POD/DMD modes offered a better resemblance of their spectral behavior when the temporal mean was removed from the original V matrix in both cases, so this additional preconditioning was applied before performing any modal decomposition.

#### 2.6.2. POD

Proper Orthogonal Decomposition reduces the flow in a set of spatially-orthogonal modes that capture the maximum amount of energy related to the oscillations of a relevant variable of the flow field (e.g., pressure or velocity) in a certain number of modes. The purpose of this technique is the identification of a finite set of deterministic shape functions that contain most of the energy in the domain. In this way, reduced order models of a complex flow could be derived from a truncated series of modes. In this case, the general expression for retrieving a random snapshot of the flow would be:

$$\xi(\bar{x}, t) - \hat{\xi}(\bar{x}) = \sum_{i=1}^{N} \Phi_i(x) a_i(t) \tag{12}$$

Where is $\xi$ is referred to the variable of the flowfield, $\hat{}$ is the temporal average, $\Phi_i(x)$ is the spatial distribution of the mode $i$ and $a_i(t)$ are the temporal coefficients associated to that mode.

From a practical point of view, a snapshot POD implementation based on the SVD decomposition of the preconditioned V matrix has been used. All the required information for performing this modal analysis can be directly retrieved from the matrices $U$, $\Sigma$ and $W^T$ of Eqn. (10). The columns of $U$ are related with the spatial distribution of the modes along the domain ($\Phi_i$(x) of Eqn. (12)), while the temporal coefficients of each of them ($a_i(t)$) can be obtained from the rows of the resultant matrix $\Sigma W^T$.

One of the main advantages of this technique is that it offers an automatic ranking of their relevance through the single values contained in $\Sigma$. However, the modes are not temporally orthogonal, so several frequencies can be contained in the temporal evolution of the $a_i(t)$ coefficients.

Thus, the resultant singular values of the decomposition offer a quantifiable parameter to assess the number of modes required to model a certain amount of the total energy. A Pareto chart showing the accumulated energy and the contribution of each of them ($\sigma_i / \sum_{i=1}^{N} \sigma_i$) has been obtained for the variables of interest in Fig. 4.

A relevant amount of accumulated energy on the first modes would be observed if some dominant behavior in the chamber appears. Some of these modes should also show a discontinuity in their energy with respect to the rest to prove their relevance. However, the amount of energy retrieved on the first modes is usually much lower in turbulent flames than in laminar applications due to the complexities of the flow. A relevant proportion of the total energy was contained in the first 10 modes (10-22.5%) of Fig. 4 for all the variables, so the temporal coefficients associated to these modes were analyzed in Sec. 4.2 consequently. The largest discontinuities in the unsteady energy per mode were also observed for

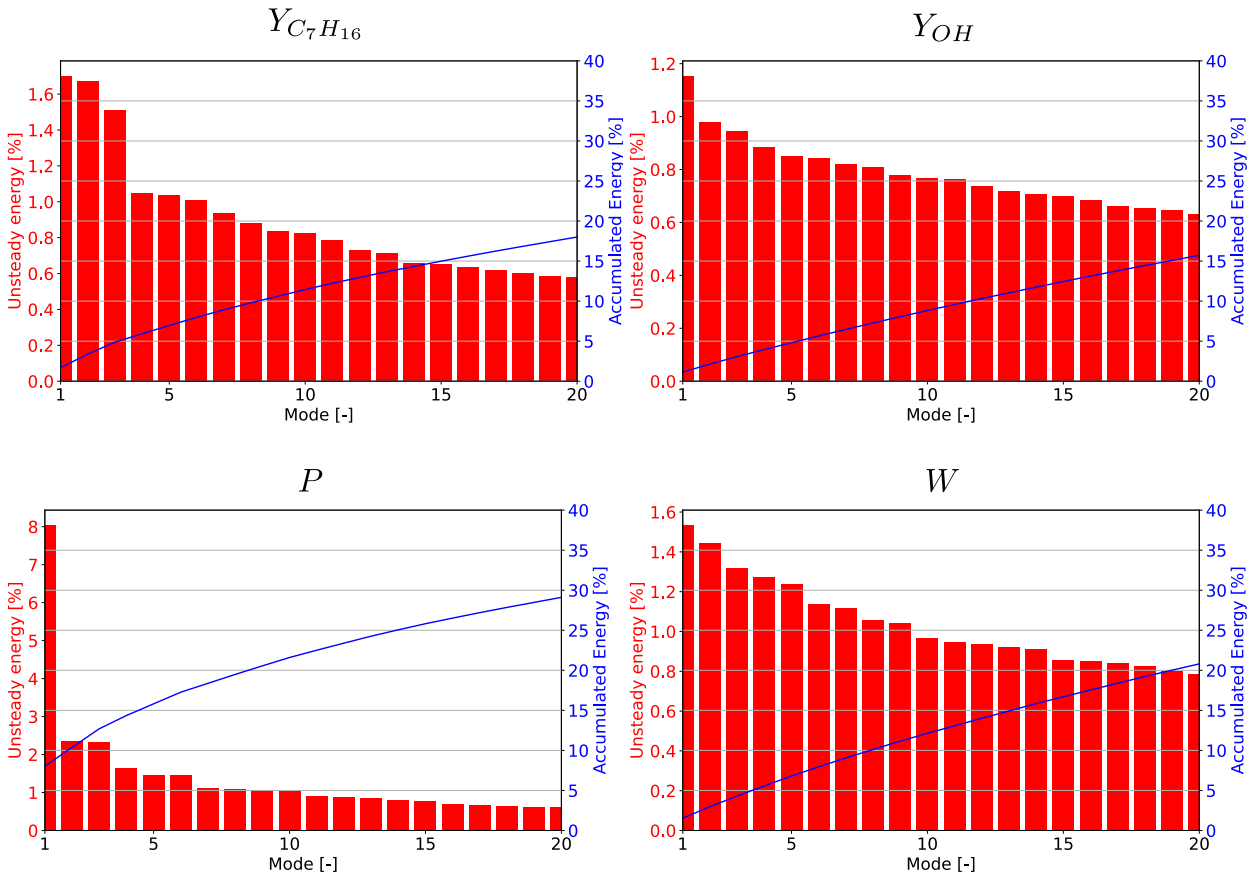


**Fig. 4.** Pareto chart showing the accumulated energy and the mode contribution for the 20 first modes in the 8-mm case.

the first 5 modes of the variables of interest (particularly in $Y_{C_7H_{16}}$ and $P$). Thus, the spatial structures of these modes were analyzed in Sec. 4.2 to see if any insightful physical phenomena could be associated. OH mass fraction and axial velocity were more transport dominated, even if the total amount of energy retrieved in the first 10 modes for the latter was larger and some coherent spatial structures could still be retrieved.

### 2.6.3. DMD

Dynamic Mode Decomposition technique is similar to the previous one but, instead of decomposing the flow into a set of spatial orthogonal basis that maximize the amount of captured energy, it looks for the dynamic content associated to a certain frequency and growth rate. The algorithm was originally elaborated by Schmid [35] and the implementation used in this work was based on [36].

This technique tries to establish a linear relation ($A$) between the flowfield snapshot $\bar{v}_i$ and the next instant of time $\bar{v}_{i+1}$, as it can be observed in Eqn. (13). $V_2^N$ expresses the snapshot matrix from $\bar{v}_2$ to $\bar{v}_N$, while $V_1^{N-1}$ was the one from the first snapshot to $N-1$.

$$V_2^N = AV_1^{N-1} \tag{13}$$

Performing a Singular Value Decomposition like the one in Eqn. (10) with the matrix $V_1^{N-1}$ and rearranging the resultant expression, a self-similar matrix ($\tilde{S}$) can be obtained:

$$\tilde{S} \triangleq U^T V_2^N W \Sigma^{-1} = U^T AU \tag{14}$$

The eigenvalues of this matrix are identical to the ones in A, but in a reduced array that is faster to solve. The spatial distribution of these DMD modes ($\Phi$) can be obtained projecting the eigenvectors of $\tilde{S}$, gathered in matrix $Y$, into U:

$$\Phi = UY \tag{15}$$

After that, amplitudes must be recovered from the normalized spatial distribution of the modes choosing the first snapshot of the flow ($\bar{v}_1$). Thus, the resultant expression for the amplitude vector ($\alpha$) is:

$$\bar{v}_1 = \Phi\alpha \tag{16}$$

$$\alpha = \Phi^{-1}\bar{v}_1 = Y^{-1}U^T\bar{v}_1 \tag{17}$$

Even if DMD is not specifically intended for reduced order models due to the low amount of energy content captured for each frequency, the information of the $V$ matrix after $k$ instants of time can be reconstructed using the temporal behavior contained in the eigenvalues of the mode ($\lambda_i$):

$$V(\mathbf{x}, t_k) = \mathbb{R}\left\{\sum_{i=1}^{N-1} \Phi_i(\mathbf{x})\alpha_i\lambda_i^{k-1}\right\} \tag{18}$$

Where $\mathbb{R}$ is the real part of the expression. The single frequency associated to each of the modes ($f_i$) can be deduced from their eigenvalues:

$$f_i = \frac{\omega_i}{2\pi} = \frac{\Im\{\ln\lambda_i\}}{2\pi\,\Delta t_{DMD}} \tag{19}$$

Where $\Im$ denotes the imaginary part of the eigenvalue and $\Delta t_{DMD}$ is the constant time step between snapshots. However, one of the main drawbacks of this algorithm is that the resultant modes are

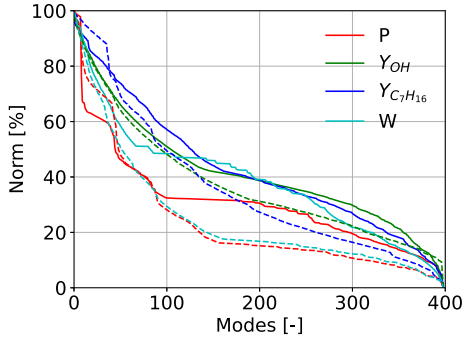


**Fig. 5.** Convergence trends of the Frobenius norm when additional modes are added to the DMD reconstruction. **Straight lines:** 8-mm case. **Dashed lines:** 12-mm case.

not classified according to the relevance of their dynamic content. An additional criterion is required to rank the relevance of these modes, Kou & Zhang [37] method was used in the previous works of the authors with satisfactory results. Hence, the same criterion was used in this numerical campaign. The expression for the relevance of each mode ($E_i$) is:

$$E_i = \sum_{k=1}^{N} |\alpha_i \lambda_i^{k-1}| \|\Phi_i\|_F^2 \Delta t_{DMD} \tag{20}$$

Where $\|.\|_F$ is related to the Frobenius norm. DMD offers a finite-dimensional approximation of the Koopman operator in nonlinear systems, like the one solved in these CFD simulations, with a certain margin of error. This approximation is valid when the considered set of linearly independent instants of time is large enough to express the next one as a linear combination of the previous ones [35]. Thus, it is reasonable to think that a convergence plot should be elaborated to see how the addition of new modes ($i$ term in the Eqn. (18)) can affect the reconstruction of the V matrix. If the nonlinear behavior of the system could be expressed in a finite-set of DMD modes, it should be observed that the Frobenius norm expressed in Eqn. (21) flattens for the addition of the response of more modes.

$$100 \frac{\left\| V_1^{N-1} - \mathbb{R}\left\{ \sum_{i=1}^{N-1} \Phi_i(\mathbf{x}) \alpha_i \lambda_i^{k-1} \right\} \right\|_F}{\left\| V_1^{N-1} \right\|_F} \tag{21}$$

Where $k \in \{1, \ldots, N\}$ and it is related with the snapshot index. The convergence trends for all the considered variables in both thermoacoustic cases (with 8- and 12-mm base size) were represented in Fig. 5.

It can be observed in this figure that the error of the approximation of the flow behavior with a linear operator was substantially reduced after considering the reconstruction with the first 100 modes. The error reduction flattens for all the variables from the 150 mode to the 300, while the error progressively became negligible for the last segment. It could be concluded that the error became well bounded from the mode 200, approximately achieving the linear independence from that point. Then, the 400 snapshots considered in this paper were enough to approximate the behavior of the nonlinear system with the DMD hypothesis.

## 3. Numeric results: validation of reactive simulations

### 3.1. Mesh quality

LES turbulent models solve all the eddies in the flow larger than a certain threshold, the smallest turbulent structures that fall below that value are calculated with a sub-grid model. Thus, a quality criterion assessment is required to see which turbulent scales can be solved. The turbulent kinetic energy criteria formulated by Pope [38] was used in this case. It is the ratio of the resolved turbulent kinetic energy ($TKE_R$) with respect the total value ($TKE_{SGS} + TKE_R$), where $TKE_R$ was derived from the fluctuations of the components of the velocity ($TKE_R = 1/2(U_{RMS}^2 + V_{RMS}^2 + W_{RMS}^2)$). LES results are generally accepted for any mesh that shows consistent quality values above 0.8. In this case, the resolution of the turbulent kinetic energy seemed to be nearly ideal (close to 1), as it can be seen in Fig. 6. Quality values tended to 0 close to the swirler walls due to the lack of fluctuations as the flow approached the no-slip velocity condition. The computation of this parameter was also performed for the coarsest cases to ensure that this quality criterion stayed above this threshold.

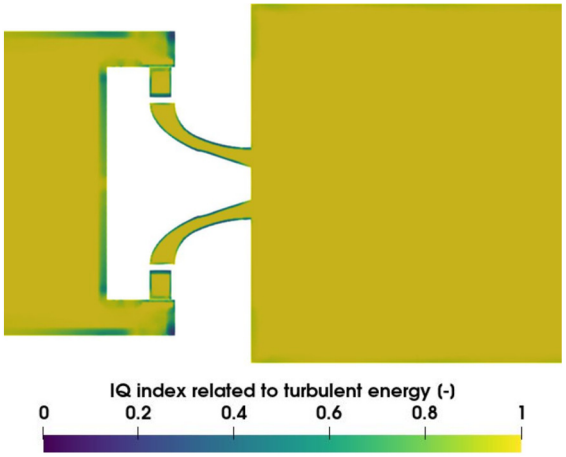


**Fig. 6.** LES quality index of the resolved TKE for the 8-mm case.

### 3.2. Velocity profiles of the gaseous phase

The results of the carrier phase were compared with the PDA measurements along the different stations where the experiments were performed [17]. The agreement of the numerical results with respect the experiments was acceptable according to the comparison shown in Fig. 7. RMS results perfectly matched the experimental results for both velocity components, proving the suitability of the grid size for capturing these fluctuations. The resultant profiles decreased downstream due to the dissipation of the turbulent structures generated close to the injection plane by the swirler. However, the magnitude of the perturbations and their profile remained nearly constant for all the axial stations. The expansion of the flow and the energy transfer from the liquid phase to the hydrodynamics led to higher turbulent intensity values that required a longer distance to dissipate. However, the divergence of the numerical results regarding the experimental measurements increased with the base size. A plausible explanation could be that the subgrid contribution to the result was not included in the RMS value. Hence, the intensity of the resolved turbulence was more underestimated in the coarsest mesh than the others.

Regarding the mean velocity components of Fig. 7, the maximum value of both velocity components increased with respect to the non-reactive regime [21] due to the aforementioned expansion in reactive conditions. The peak associated to the swirl jet was still captured properly, even if the magnitude was slightly underestimated with respect to the experimental value. The width of the jet and the presence of a central recirculation region was still well reflected. However, the magnitude of the recirculation velocity in the central region was clearly overestimated, decreasing the difference as the refinement in the injection cone increased (0.375 mm,

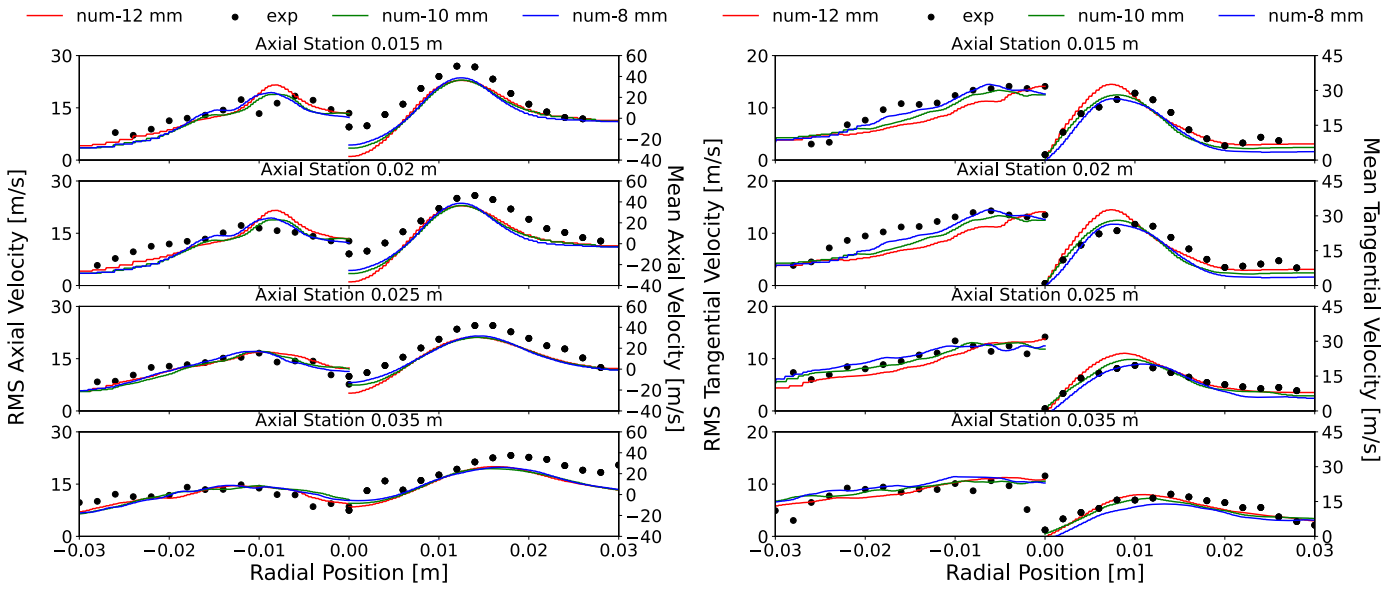


**Fig. 7.** Mean and RMS velocity components of the carrier phase. Experimental results (exp) [17] compared with respect to the numerical ones with a base size of 8, 10 and 12 mm (num - 8 mm, num - 10 mm and num - 12 mm respectively).

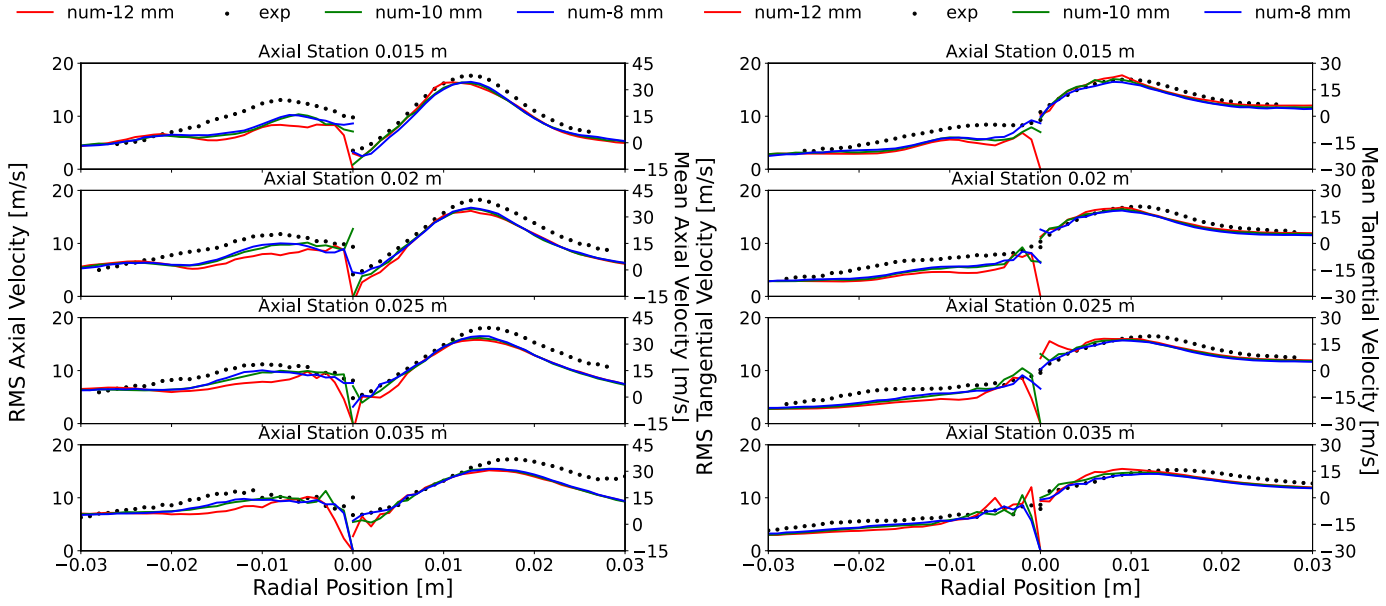


**Fig. 8.** Mean and RMS velocity components of the liquid phase without separating the statistics according to the diameter of the droplets. Experimental results (exp) were compared with respect to the numerical ones with a grid base size of 8, 10 and 12 mm.

0.3125 mm and 0.25 mm respectively). Regarding the tangential velocity, the velocity profile reflected the clockwise rotation of the flow and the increment of the maximum value due to the thermal expansion. Numerical results tended to the experimental ones when the grid was refined.

### 3.3. Velocity profiles of the dispersed phase

Regarding the dispersed mesh, the adjustment of the parameters of the spray was already done in the previous work of the authors [21]. The convergence of the velocity trends was assumed due to the elevated amount of injected parcels and the long time spent for averaging. First, the numerical velocity profiles at the different stations were compared with respect to the experimental results without separating the statistics in different groups of diameter bins in Fig. 8. The outer angle of the injection cone and the velocity peak seemed to be slightly underestimated according to the comparison. The lower magnitude observed in the velocity peak of the carrier phase probably had a relation with this fact. However, the fitting seemed to be nearly perfect close to the injection plane and the observed deviations in the far-field were within the acceptable margins compared to other simulations done in this combustor [39].

Another interesting aspect that could be observed in these results was that the RMS components were underestimated for all the velocity components. Sauter Mean Diameter was clearly overestimated in all the axial stations (Fig. 9), most of the parcels had a characteristic diameter larger than expected. This fact irremediably influenced the intensity in the fluctuations of the velocity due to the reduced sensitivity that large parcels had with respect to the motion of the flow. The presence of these large numerical droplets could be related to the absence of a boiling model that comple-

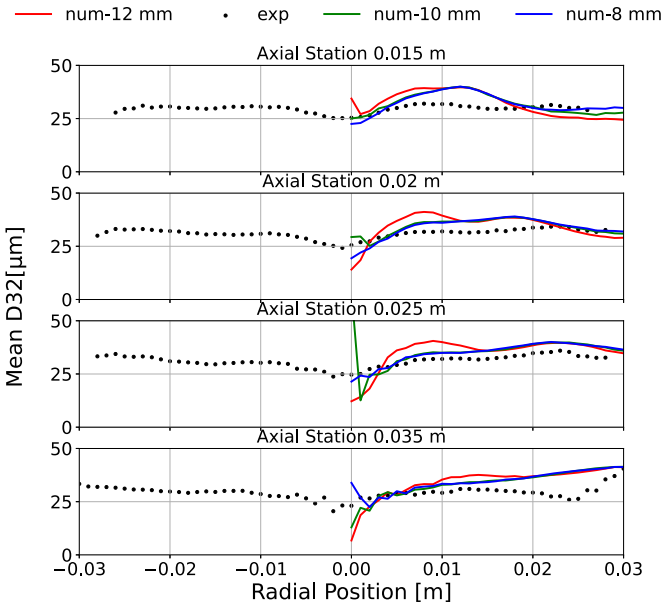


**Fig. 9.** Sauter Mean Diameter of the numerical parcels at different axial stations where the experimental data were recorded (exp).

mented the evaporation model. The change of the radius of the droplets was only modeled until the droplet temperature achieved the boiling point. A further droplet size reduction would have been obtained if this model had been activated and the estimated SMD would have been probably improved. However, the correspondence of these results with respect to the experimental measurements was good, so the simulation setup was accepted. This possibility will be studied in future works.

### 3.4. OH contours

This stabilized flame configuration was already studied in [39, 40]. However, a correct resolution of the combustion and a stabilization of the numerical flame was required to calculate the acoustic simulation. Thus, the numerical OH contours obtained along the central plane were compared with respect to the measurements done with the OH-PLIF in the aforementioned works of the literature. Mean and RMS were obtained using both methodologies. Regarding the experimental part, it was computed from 1000 images, reader is referred to [17] to know more about these measurements. The numerical statistics of this radical were computed during 100 ms as it has already been mentioned. The results of the three LES were compared in Fig. 10 to assess the effect of the resolution on the computation of this species.

Numerical mean flame was nearly identical to the experimental one regardless of the mesh resolution. Despite this, some differences could be observed between them. All the cases were capable of properly reproducing the M-shape of the flame, reflecting its lift perfectly. However, the penetration of the swirl jet increased with the mesh resolution. This was probably related to the overestimation of the axial recirculation velocity of the carrier phase (Fig. 7) in the Central Toroidal Recirculation Zone (CTRZ). The numerical dissipation of the swirl jet could have influence on the reduction of the internal black regions too. Furthermore, the largest width in the central region of the flame was obtained for the coarsest mesh and progressively decreased with additional refinement. These intermediate values were related to the burnt gases that contain OH traces [40]. The numerical diffusion that the coarse mesh induced in the solution spread the hydroxyle radicals, generating a wider flame region than expected. Furthermore, the mass fraction of OH on both flame brushes was maximum close to the wall. The highest intensities in the contour were related to the post-flame front, where relevant reactivity rates take place. The lack of resolution in the flame front probably led to increase the region that contained a large mass fraction of this radical.

RMS values did not properly correspond with the experimental contour. Both had a similar shape but the tips of the contour seemed to be far away from the wall, even if it slightly improved for the 8-mm case. A plausible explanation could be that a wider part of the domain with a finer resolution was required to capture properly the fluctuations of the flame close to the combustor wall. However, the maximum resolution was determined as a trade-off between the computational cost and the accuracy of the results, as it has been previously remarked in this section. Furthermore, no thermoacoustic instabilities were present, so the oscillations in the heat release were not expected to generate a feedback mechanism with the pressure perturbations.

Finally, the numerical estimation of the lift-off height was compared to the experimental one (see Fig. 11) to see if the stabilization point of the flame was properly assessed. All the cases underestimated the lift-off height but the match of the most refined case was reasonable. Lift-off height is a multifactorial problem that depends on several parameters like the local velocity of the carrier phase, the mixture fraction, or the interaction between the droplets and the flame. Large recirculation velocities in the 12-mm case could have induced larger slip velocities on the droplets and consequently larger shear stresses acting on these particles, enhancing the evaporation and mixing of the dispersed phase. Thus, local inflammable conditions could have been achieved closer to the injection plane, reducing the height of the stabilization point of the flame.

## 4. Combustion noise analysis

The results of the modal analysis and the frequency distribution of the monitor signals were presented in this section to understand the acoustics, the combustion and the hydrodynamics in this chamber.

### 4.1. FFT results

This section shows the results obtained for the signal analysis performed from the monitor points of the acoustic simulation. As it has already been explained, these cases consisted in elongating the computations of the previously stabilized flame during 20 ms with the corresponding adjustments of the time step. One-dimensional punctual signals were collected along a 2D grid in the XZ plane using 115 lines from 0 to 230 mm with a separation of 2 mm. The separation between the monitor points in each line was 2 mm. Thus, 5750 probes were positioned along the domain to record the pressure signals. The signals were recorded with a sampling frequency of 100 kHz. Furthermore, additional positions were monitored (i.e., plenum, swirler, exhaust nozzle) to compare with the experimental results and find more information about the dominant modes in the system. These results can be observed in Fig. 12.

The Fast Fourier Transform of the signals was performed to analyze the frequency content with the maximum resolution ($\Delta f = 50$ Hz) along the locations of the chamber. The experimental one was recorded at the exhaust nozzle with a sampling frequency of 10 kHz during 0.7 s, obtaining a $\Delta f$ of approximately 1.43 Hz. These pressure oscillations were recorded from the ignition until the stabilization of the flame, so a spectrogram of the experimental signal was computed to see if any variation of the dominant frequencies was produced over time. It was observed that the intensity of the dominant peaks was fully stabilized from 0.2 s, so

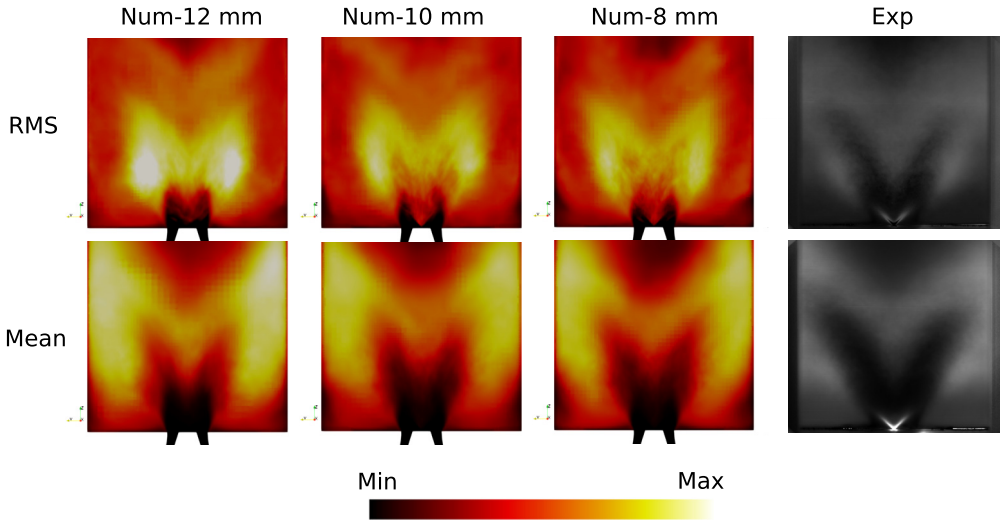


**Fig. 10.** Comparison of Mean and RMS OH contours between all the numerical (num) and the experimental measurements (exp) [17]. The maximum $Y_{OH}$ was 0.024 in these contours, while the minimum was null. The size of the experimental image was 94 × 94 mm.

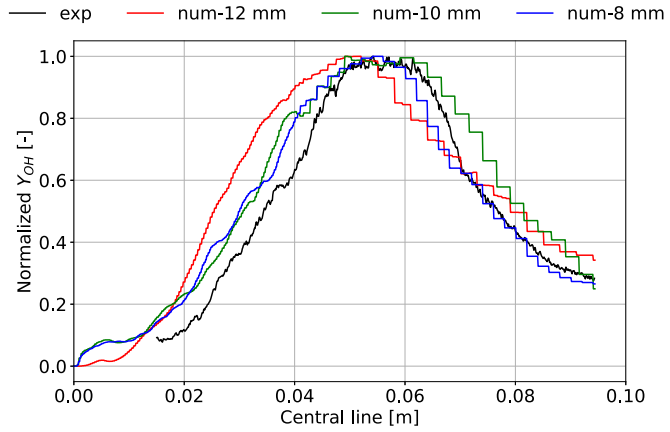


**Fig. 11.** Comparison along the central axis of the burner between the numerical $Y_{OH}$ and the experimental results (exp) to assess the accuracy of the computed lift-off height. The numerical results are plotted between [0,0,0] mm and [0,0,94] mm.

the first 2000 points were not considered in the FFT postprocessing.

Despite this, the difference in resolution between the experimental and the numerical signal was too large. For this reason, the experimental signal was divided in segments of 20 ms where the DFT was computed. Finally, those frequency distributions were averaged to obtain a representative spectrum with the same $\Delta f$ as the simulations.

The units of the experimental pressure oscillations, or even if the signals were amplified with a certain factor, were not known in this case, so the spectral content in both cases was normalized with respect to the maximum peak to be able to compare them. Three dominant peaks could be observed in the experimental signal: 300 Hz, 450 Hz, and 1200 Hz. These dominant peaks could correspond to hydrodynamic phenomena already observed in [21]. Particularly, the dominant frequency at 300 Hz could be related to the presence of a Vortex Breakdown Bubble of the Central Toroidal Recirculation Zone, while the 1200 Hz was nearly identical to the dominant frequency of the previously observed Precessing Vortex Core. The 450 HZ experimental peak could not be identified in the numerical simulations and its nature could not be determined. Despite this, the 300 Hz numerical peak at the Position 6 seemed to appear also for other probes in the domain, so further investigation of this mode was required to understand its nature.

The mismatch in the peak amplitudes at probe 6 with the experiments could be due to several reasons. Agostinelli et al. [41] proved that the heat transfer modeling through the combustor walls was a relevant aspect to accurately recover the thermoacoustic behavior of a premixed chamber. CHT simulations could be recommended for this type of cases, but they require detailed experimental simulations and a large computational effort that were out of the scope of this paper.

Another important factor could be the resolution at the flame front. Silva et al. [42] remarked that a plausible explanation for the difference of the numerical global heat release and the pressure frequency distributions that they observed when the mesh refinement was varied could be the lack of resolution for the smallest turbulent scales at the shear layer. This could affect the generation of the largest coherent scales in the chamber, and consequently the combustion and acoustic fields. In this case, the relevance of the hydrodynamic peaks seems to be affected by the mesh resolution, so this could be also a possible explanation for this case.

Finally, the complexity of properly measuring these phenomena experimentally should also be considered. The pressure transducer was located at the exhaust nozzle with a copper duct attached to the wall to avoid the direct interaction of the exhaust gases with the sensor. The numerical amplitude of the dominant frequencies were 120 Pa, 38 Pa and 7 Pa respectively for the 300, 1200, 2000 Hz modes respectively. Thus, it is reasonable to think that any small damping effect that the duct could be inducing is going to notoriously affect the presence of the experimental hydrodynamic peaks in the frequency distribution. This is the most plausible explanation to justify the amplitude mismatch on those frequencies.

The FFT of the signal computed at probe 1, which was positioned at the plenum, showed a single dominant frequency at 300 Hz. This peak was identical to the one observed in the comparison with respect to the experimental results. The plenum made the flow uniform before getting into the domain, so no hydrodynamic modes should have appeared in this region. Thus, this mode was also related to the acoustic motion that propagated from the chamber to the inlet, more details about this mode and its nature will be studied in subsequent sections of the paper. Regarding the second position, the probe was placed inside the swirler channel, so a larger energetic density was found in this narrow space.

The monitor point was close to the origin of the PVC, so its effects were captured in the dominant frequencies of the signal. Monitor point number 3 was positioned in the outer shear layer of the swirl jet. PVC is originated due to the precession of the CTRZ

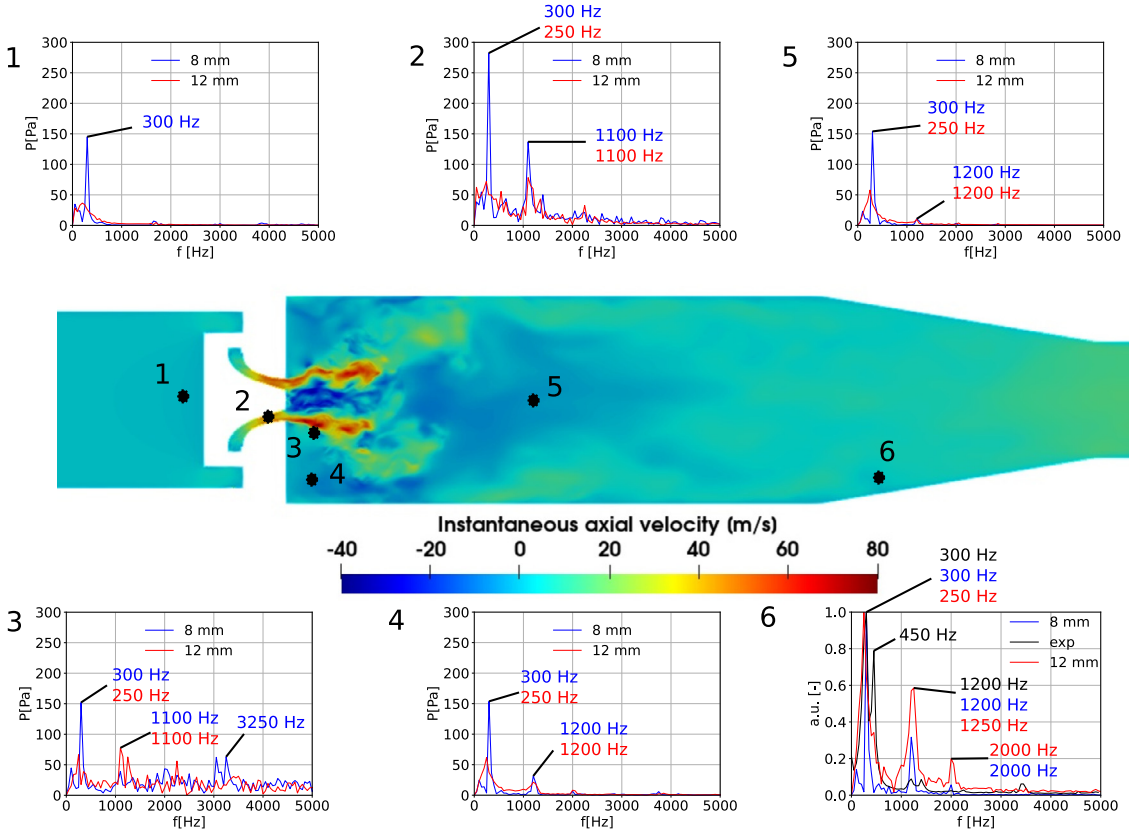


**Fig. 12.** FFT of the pressure signals computed in the chamber. Sampling frequency was 100 kHz and they were recorded during 20 ms ($\Delta f = 50$ Hz). The black line in position 6 is the experimental frequency distribution. **Position 1**: plenum [0,0,−50] mm, **Position 2**: swirler [0,8,−5] mm (not in this plane but added for illustrative purpose), **Position 3**: swirl jet [15,0,10] mm, **Position 4**: corner recirculation zone [45,0,10] mm, **Position 5**: combustor [0,0,120] mm, **Position 6**: exhaust nozzle [40,0,310] mm.

that interacts with the shear layer of the swirl jet and generates helical coherent flow patterns that propagate in the chamber. Thus, this probe was perfectly positioned to detect the influence of the PVC. First, second and third harmonics appeared for both refinements, showing another evidence of the existence of this pattern for the CORIA Spray LDI burner in reactive conditions. Furthermore, the local effects of the hydrodynamic modes in the pressure oscillations were confirmed analyzing the signals obtained in probes 4 and 5. The dominant frequencies associated to the second and third harmonic of the PVC nearly disappeared for the 4th probe, while only the dominant peak associated to 300 Hz was relevant in the graph of the 5th one.

Besides this, the narrowband nature of the hydrodynamic phenomena can also be observed in the frequency shift of the dominant frequency associated to the Precessing Vortex Core depending on the monitor location (1100-1200 Hz).

### 4.2. POD

Proper orthogonal decomposition was obtained from the variables previously mentioned to find more information about the interactions that exist between them. As it can be observed in Fig. 13, only the temporal coefficients of the first 10 modes were represented.

Fig. 13 first column showed that multiple dominant frequencies appeared for the fuel mass fraction. Modes $\Psi_1$ and $\Psi_2$ had a dominant frequency at 1100 Hz that was associated to the appearance of PVC. Thus, this hydrodynamic mode seemed to play a relevant role in the mixture of the fuel mass fraction with the gaseous phase in reactive conditions. Furthermore, it was observed in [21] that these modes usually appeared in pairs. In this case, similar hydrodynamic structures seemed to appear during combustion. However, there was a remarkable difference in the results depending on the mesh refinement. $\Psi_3$ had a dominant peak at 300 Hz for the case with a base size of 8 mm, while it seemed to vanish for the coarsest case. The spectral content of the modes $\Psi_{4-5}$ coincided with the dominant frequencies seen for $\Psi_{3-4}$ of the coarsest mesh, so the aforementioned mode could not be recovered in this case. Thus, hydrodynamic modes and their corresponding frequencies were properly captured for both meshes, while the effect of the 300 Hz was damped in the coarsest mesh. The numerical dissipation effects of the largest mesh could be promoting this behavior.

The relevance of the frequency associated to the PVC mode changes between both mesh refinements for the OH mass fraction. It could be observed that it became dominant in $\Psi_{4-5}$ for the coarsest mesh. Lack of resolution in the flame front could have led to a miscorrelation in the reactivity of the shear layer that gave additional relevance to the PVC in the combustion behavior. Despite this, it can be observed that this frequency slightly influences the mass fraction of OH for the most refined case, affecting several modes.

Regarding the FFT of the temporal coefficients associated to the pressure modes, the resultant behavior was expected (see Fig. 13 third column). In the end, the pressure oscillations take into account the acoustic and the hydrodynamic part, so all the dominant frequencies of the pressure signals collected in the cells close to the injection plane were expected to belong to one of them. First, second and third PVC harmonics (1100 Hz, 2100 and 3150 Hz) were present for $\Psi_{2-3}$, $\Psi_{5-6}$, $\Psi_{7-8}$, while the highest harmonics disappeared for the coarsest case. The relevance of the acoustics in

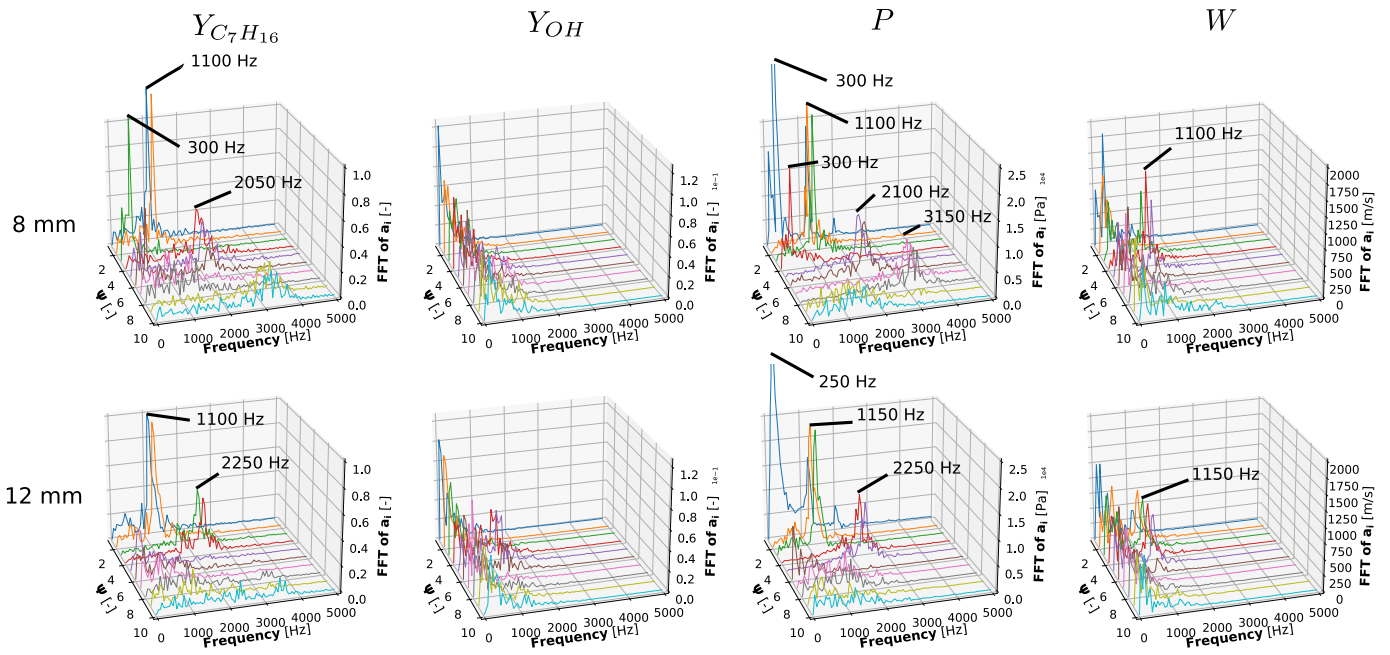


**Fig. 13.** FFT of the temporal coefficients of the first 10 POD modes obtained, the frequency resolution is 50 Hz.

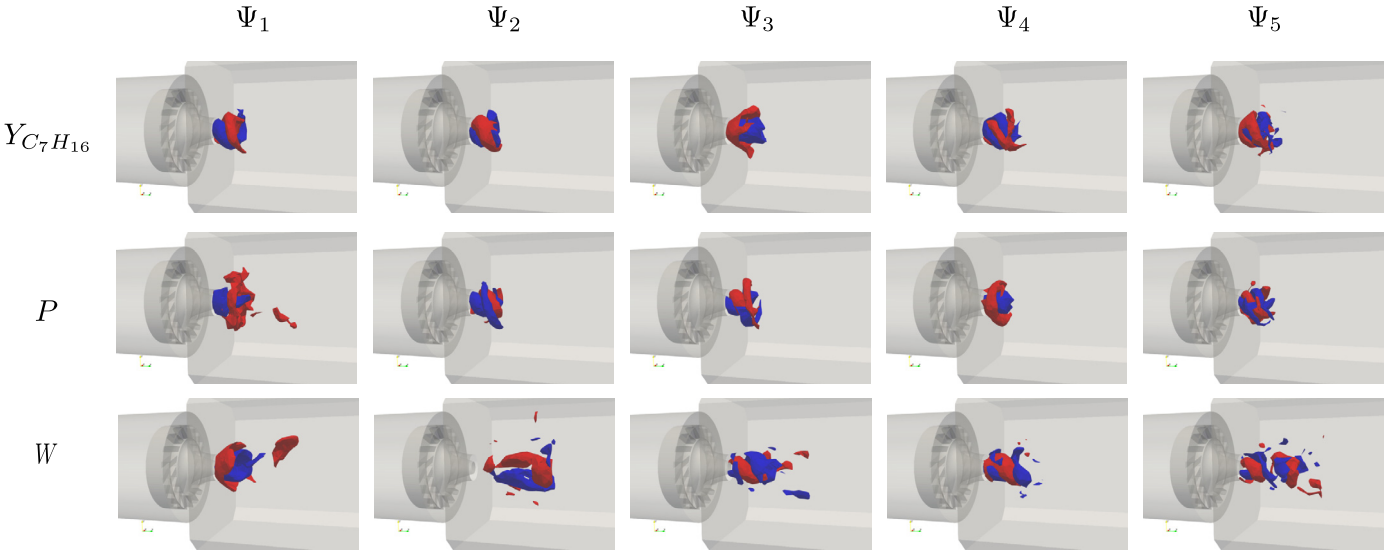


**Fig. 14.** Spatial distribution of the modes $\Psi_{1-5}$. Blue color represents the percentile 2% of the energy distribution of the real values in the mode, while the red one is the percentile 98%. (For interpretation of the colors in the figure(s), the reader is referred to the web version of this article.)

the temporal evolution of the modes associated to the most refined mesh was proven again in the modes $\Psi_1$ and $\Psi_4$ of this variable.

Finally, dominant modes of $a_i(t)$ for the axial velocity were identical regardless of the base size. Besides low-frequency content associated to the turbulence, the dominant frequency of the PVC appeared, showing that this dynamic phenomena was involved in all the processes of mixing and stabilization of the flame.

Spatial distributions of the first five modes of $Y_{C_7H_{16}}$, $P$, and $W$ were represented in Fig. 14. It could be observed that pressure and fuel mass fraction were still correlated in reactive conditions through the hydrodynamic coherent structures. Modes $\Psi_{1-2}$ of $Y_{C_7H_{16}}$ showed a single helical structure that matched the shape of a typical PVC. Furthermore, both modes were shifted $\pi/2$ from each other, confirming that these modes usually appear in pairs with a certain phase lag between them. Similar structures were observed in modes $\Psi_{2-3}$ of pressure. This also happened for the harmonics of the PVC, showing double helical structures shifted $\pi/2$ at $\Psi_{3-4}$ of $Y_{C_7H_{16}}$ and $\Psi_{5-6}$ of P. Another interesting structure was the one of $\Psi_2$ in the fuel mass fraction row, the spatial distribution contains the swirl jet and the central recirculation zone of the flow, so it could be associated to the Vortex Breakdown Bubble. Similar structures could also be observed in $\Psi_1$ and $\Psi_4$ of the pressure. Regarding the spatial distribution of the axial velocity modes (see last row in Fig. 14), same kind of helical structures could be observed in $\Psi_{2-5}$, while a state similar to the Vortex Breakdown Bubble was still observed for $\Psi_1$. However, these structures seemed to extend along a wider range of the domain than for the other two variables. The thermal expansion of the flow velocity in reactive conditions was probably related to this fact.

Finally, the influence of the mesh resolution in the representation of these phenomena through POD was illustrated in Fig. 15. It could be observed that an helical coherent structure was captured for the $\Psi_5$ mode of $Y_{OH}$ in the coarsest mesh, while no structures could be distinguished in the most refined one. Lack of resolution

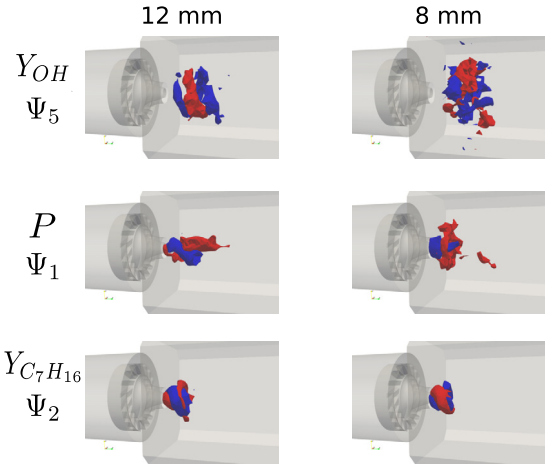


**Fig. 15.** Spatial distribution of the $\Psi_5$ mode of $Y_{OH}$, $\Psi_1$ mode of $P$, and $\Psi_2$ mode of $Y_{C_7H_{16}}$ to see the effect of the refinement.

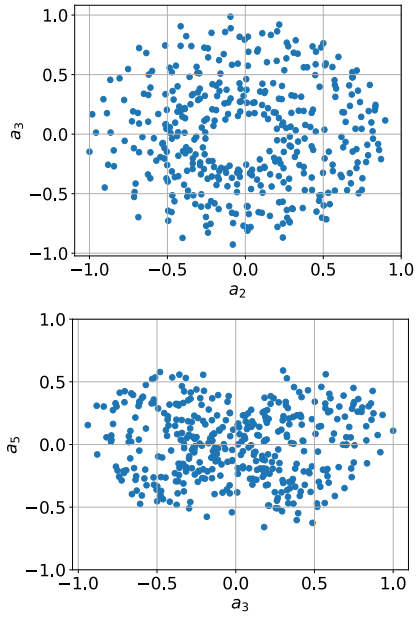


**Fig. 16.** Normalized phase portrait for the temporal coefficients associated to the different pressure POD modes ($a_i$), where $i$ denotes the mode number. The normalization was performed using the maximum absolute value of both temporal sequences.

probably enhanced the diffusion of the OH radicals that entered in contact with the hydrodynamic structures, capturing the PVC. OH is a species that is generated fast in the flame front but it also disappears early: if the resolution on the flame front was increased, the region of the space where this radical was generated and destroyed became thinner, becoming more difficult to recover coherent structures.

Furthermore, $\Psi_1$ mode of pressure was also compared between both meshes. A distorted VBB was recovered for the case with a base size of 12 mm, while a shorter coherent structure could be observed for the same mode in the most refined case. A constant number of cells was chosen to calculate the POD and the DMD regardless of the mesh size. For this reason, the probability of choosing a large amount of nearby cells that do not properly capture the extent of the mode increases with the mesh size. However, the main hydrodynamic structures could be distinguished using one million cells, even for the most refined cases. Despite the local distortion that could be obtained for a particular mode like this one, most hydrodynamic modes were unambiguously recovered for both meshes, as it can be observed in the $\Psi_2$ mode of $Y_{C_7H_{16}}$ in Fig. 15.

Finally, POD modes are a mathematical projection of the flow energy in a finite set of modes. The physical interpretation of these modes is always going to have a subjective component [43], even if it is supported on several objective parameters like the modal energy plot or the comparison of the spatial structures with the literature information. Another representation that could be useful to understand how the modes interact with each other are the phase portraits of the temporal coefficients associated to the modes. If the scatter plot of the normalized instantaneous values associated to one mode with respect to other tends to describe a Lissajous figure of a circle, it means that these signals have a periodic behavior with a $\pi/2$ phase between them, while an eight-like form could indicate an harmonic relation [44].

According to the previous description, Fig. 16-top show a periodic behavior between the modes $\Psi_2$ and $\Psi_3$ of the pressure with the aforementioned phase difference. This pattern was also obtained for the modes $\Psi_{1-2}$ of $Y_{C_7H_{16}}$ and $\Psi_{5-6}$ of pressure, but the representations were not included to avoid redundant information. Besides this, Fig. 16-bottom represents the harmonic relation that exists between modes $\Psi_3$ and $\Psi_5$ of pressure. The same pattern was found between $\Psi_1$ and $\Psi_4$ of the fuel mass fraction. Thus, these representations provide an additional evidence to support that the different modes obtained from the considered variables of interest have a deterministic behavior.

### 4.3. DMD

Dynamic Mode Decomposition was also performed for $P$, $Y_{C_7H_{16}}$, $Y_{OH}$ and $W$. The rank of the modes was obtained with the Kou & Zhang criterion [37] for the 8-mm case (see Fig. 17) and normalized with respect to the highest value found in the modes. The dynamic content in Fig. 17 closely resembles the frequency distribution of the temporal coefficients associated to the POD modes of Fig. 13. A progressive decay in the relevance of the modes can be observed for all the variables as the frequency associated to them increases. This proves the influence that the low-frequency dynamics have on this type of combustion chamber.

The influence of the PVC harmonics can be observed in the DMD rankings of the pressure and fuel mass fraction. The 300 Hz mode associated to the VBB is the most dominant frequency for the pressure in this technique too, while the predominance of the PVC for the $Y_{C_7H_{16}}$ is also observed. The OH mass fraction did not show any relevant mode in the ranking probably due to the absence of coherent structures in the chamber. The DMD ranking for the axial velocity proved the influence of the PVC and its harmonics on the dynamic content of this variable of interest, as it was observed in Fig. 13 too.

After this, the spatial distribution of the modes associated to the most dominant frequency bands of the DMD rankings were studied to see if any coherent structure could be retrieved (Fig. 18). It must be remarked that the hypothesis of recovering modes whose temporal evolution is determined by the real and imaginary parts of their eigenvalue complicates the projection of the dynamic content into a set of temporally orthogonal modes. However, a coherent structure that could be associated to the Vortex Breakdown Bubble appeared for 300 Hz mode of the axial velocity, pressure and fuel mass fraction. First and second PVC harmonics (1150-1000 and 2150 Hz respectively) appeared for the two latter variables, corroborating the role of this helical structure in the hydrodynamic component of the pressure oscillations and the mixing processes of the chamber. The third harmonic of the PVC was also obtained for the pressure (3250 Hz) and the fuel mass frac-

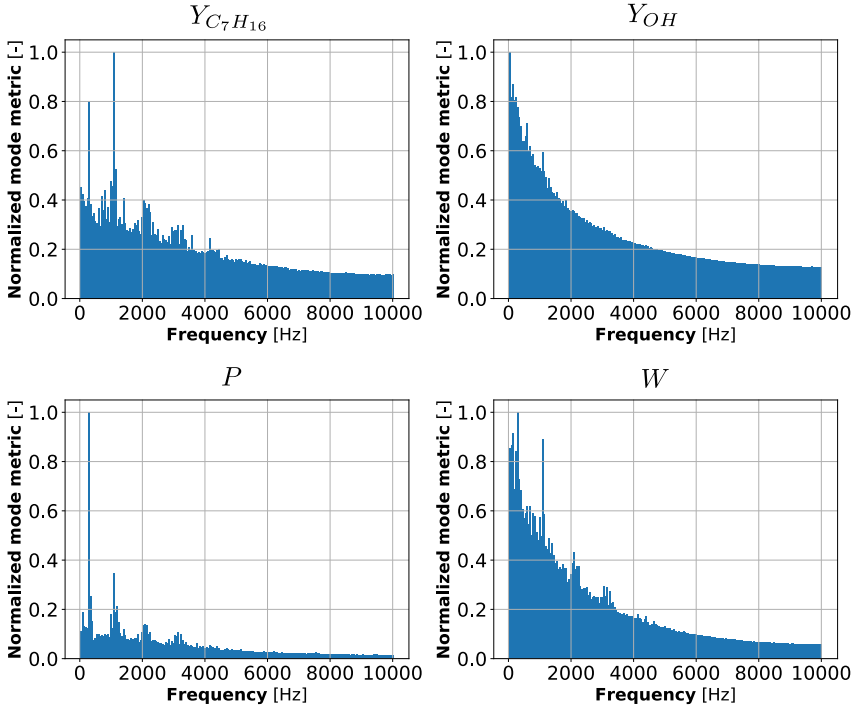


**Fig. 17.** Ranking of the DMD modes using the Kou & Zhang criterion.

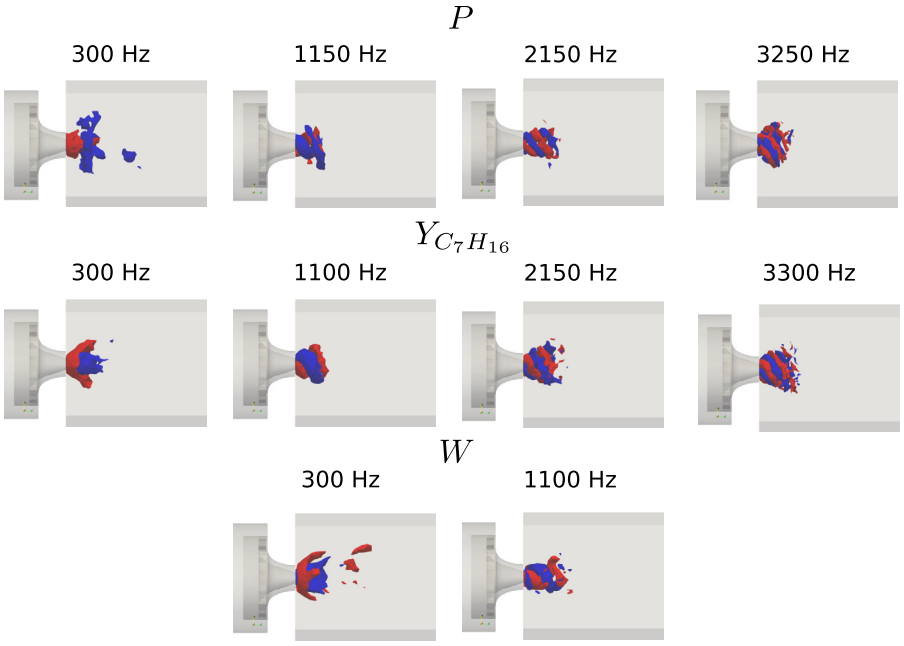


**Fig. 18.** Spatial structures of the most relevant DMD modes obtained for $Y_{C_7H_{16}}$, $P$ and $W$. The dynamic content of the real part of the mode was split in the 98-2% percentiles, represented in red and blue respectively.

tion (3300 Hz). No coherent structures could be observed for the OH mass fraction close to the VBB and PVC frequencies.

Even if only a few modes could be recovered from the DMD, the information provided by this technique was very useful. POD showed that the VBB and the PVC were the most energetic structures in the flowfield. However, the information about the temporal behavior of these phenomena was limited due to the inability of the POD to ensure the temporal orthogonality of the modes. DMD provided modal spatial distributions similar to the ones obtained through the POD. This proved that a linear relation could be established to model the temporal evolution of these complex phenomena. Thus, the information provided by both algorithms was complementary and could be very useful to generate reduced order models that help to simplify the dynamics that take place in the chamber.

### 4.4. Helmholtz solver analysis

The natural modes of the geometry were computed using ANSYS modal acoustics to find if some of them induced resonance in the dominant frequencies observed for the hydrodynamic modes. An homogeneous expression of the Helmholtz equation was solved

**Table 1**
Natural frequencies of the first 10 modes of the chamber in reactive conditions.

| Mode | Frequency [Hz] |
|---|---|
| 1 | 181 |
| 2 | 310 |
| 3 | 1225 |
| 4 | 1704 |
| 5 | 2068 |
| 6 | 2719 |
| 7 | 2719 |
| 8 | 2909 |
| 9 | 3049 |
| 10 | 3141 |


**Fig. 19.** Spatial distribution of the natural mode obtained 310 Hz.

in this case, considering the properties of the flow (i.e., speed of sound and the heat capacity ratio) to be constant on different regions of the domain. Thus, it was assumed that the unsteady heat release did not act as an active generator of pressure perturbations in this case to find the eigenmodes of the chamber. However, authors want to acknowledge the relevance of the unsteady combustion on the acoustic field in this kind of burners and the necessity of considering this nonlinear term in the Helmholtz equation [4], but this hypothesis has also been widely considered in the literature [14,45] to solve the eigenproblem for this kind of applications. For this reason, the validity of the hypothesis was assumed in this work.

The reservoir appended to the geometry during the CFD calculations was excluded in this case to avoid the possible distortion of the natural frequencies of the system. It was assumed that the domain was filled with air but at different states. Particularly, the air in the plenum and the swirler was assumed to be at $P = 1$ atm and $T_{air} = 416$ K, obtaining a speed of sound of 409 m/s ($c = \sqrt{\gamma RT_{air}}$). The state inside the combustion chamber was different. According to the CFD calculations in reactive conditions, the mean temperature was assumed to be 1400 K, while $\gamma = 1.3$. Thus, the speed of sound was approximated as 723 m/s. All the boundary conditions were supposed to behave as rigid walls except the outlet surface at the exhaust nozzle, where an open boundary condition was imposed ($P' = 0$). The latter was assumed to be reasonable due to the atmospheric outlet of the experimental facility. However, this assumption is not always correct and acoustic impedances must be considered in other cases (e.g., for the computations of a real combustion chamber).

The resultant natural frequencies can be observed in Table 1. The first five modes corresponded to the longitudinal motion of the acoustic waves, while the last five were related to mixed modes.

The second mode had a similar frequency with respect to a dominant peak observed through the postprocessing techniques applied on the LES simulations. FFT of the punctual measurements showed a consistent peak at 300 Hz presumably related to the VBB, while the results of POD and DMD proved its existence for the pressure and fuel mass fraction fields. Thus, this acoustic mode could have induced the resonance of the VBB and the amplification of its relevance close to the injection plane.

Fig. 19 shows the spatial distribution of the natural mode. It reflected a coupling between the combustion chamber and the plenum due to the observed propagation of the acoustic wave on both ducts indistinctly. The spatial distribution of the mode tended to be a 1/4-wave along the combustion chamber.

## 5. Conclusions

A numerical setup for reactive simulations in gas turbines was validated in CONVERGE using the experimental results obtained at the CORIA Rouen Spray LDI burner. The overall fitting between the velocity profiles and the OH contours was good, but there were some aspects like the SMD profiles or the RMS contours of the OH that still could be improved. The absence of a boiling model, or the way that the sub-grid interactions between the chemistry and the turbulence were treated, could be possible sources of error that could lead to these miscorrelations and will be studied in future papers. In these simulations, the increase of the grid size behaved as expected and the results were improved for the most refined mesh.

Regarding the thermoacoustic simulations, 1D FFT analysis confirmed the appearance of a dominant peak around 300 Hz that prevailed along the combustion chamber, while the dominant frequency associated to the PVC (1100-1200 Hz) appeared close to the swirl jet and proved the local effects of this hydrodynamic mode on the pressure. POD and DMD results evidenced the relevance of VBB and PVC in the coupling between P, W and $Y_{C_7H_{16}}$ during the reactive conditions of this combustor. Furthermore, the natural frequencies of the system were calculated and showed that a resonance may exist between the second coupled longitudinal mode in the chamber (310 Hz) and the CTRZ reconstructed from the pressure results (300 Hz). However, this mode was not observed in the POD and DMD results of $Y_{OH}$, so the unstable feedback interaction between the combustion, hydrodynamics and acoustics was not closed. Thus, PVC and VBB (particularly CTRZ) resulted to be the dominant source of combustion noise in this burner.

A summary table comparing the dominant frequencies obtained in the non-reactive cases of [21] and the reactive simulations of this paper for the fuel mass fraction and the pressure can be observed in Table 2. Dominant frequencies were nearly identical for

**Table 2**
Comparison of the non-reactive modes obtained for $P$ and $Y_{C_7H_{16}}$ in [21] with respect to the reactive ones computed in this work.

| Technique | Regime | Variable | PVC | | | | CTRZ |
|---|---|---|---|---|---|---|---|
| | | | $1^{st}$ harm. | 2nd harm. | 3rd harm. | 4th harm. | |
| POD | Non-reactive | Pressure | 1088 Hz | 2176 Hz | - | - | 247 Hz |
| | | Fuel | 1088 Hz | 2077 Hz | - | - | 49 Hz |
| | Reactive | Pressure | 1100 Hz | 2100 Hz | 3150 Hz | - | 300 Hz |
| | | Fuel | 1100 Hz | 2050 Hz | - | - | 300 Hz |
| DMD | Non-reactive | Pressure | 1105 Hz | 2215 Hz | 2970 Hz | 4475 Hz | 400 Hz |
| | | Fuel | 1085 Hz | 1692 Hz | 2995 Hz | 4675 Hz | 175 Hz |
| | Reactive | Pressure | 1150 Hz | 2150 Hz | 3250 Hz | - | 300 Hz |
| | | Fuel | 1100 Hz | 2150 Hz | 3300 Hz | - | 300 Hz |

both regimes regardless of the hydrodynamic mode considered. Thus, the effect of the reactive conditions on the modes of the chamber depends on the burner and the nature of the modes involved.

Finally, grid size had some influence on the dominant frequencies of the modes and their spatial distributions in these simulations. The resolution affected the amplitude of the dominant peaks of the FFT signals due to the numerical diffusion induced by the coarsest mesh. Furthermore, largest frequencies of the temporal coefficients related to the POD modes could not be recovered (3150 Hz peak related to pressure modes), while the resonance was not captured for the case with a base size of 12 mm neither.

## Declaration of competing interest

The authors declare that they have no known competing financial interests or personal relationships that could have appeared to influence the work reported in this paper.

## Data availability

Data will be made available on request.

## Acknowledgements

This work is part of the R+D+i project "Contribución a la aviación sostenible a través de la optimización numérica de cámaras con combustión pobre para aeromotores de nueva generación más silenciosos y limpios (QUILECOM)", reference PID2019-109952RB-I00, funded by MCIN/AEI/10.13039/501100011033. M. Rodríguez-Pastor is supported by grant PRE2020-093592 funded by MCIN/AEI/10.13039/501100011033 and by "ESF Investing in your future".

The authors want to thank Dr. Bruno Renou, Dr. Gilles Cabot and Dr. Javier Marrero for their kindness in sharing their experimental data and the fruitful discussions that ensued.

## Appendix A

The cost of the numerical simulations performed for this work can be found in Table A.1

**Table A.1**
Cost of the simulations performed during the numerical campaign in cpu-h.

| case / mesh | 8-mm | 10-mm | 12-mm |
|---|---|---|---|
| Reactive | 58345 | 28211 | 16613 |
| Thermoacoustic | 67952 | - | 14088 |

## References

[1] Y. Liu, X. Sun, V. Sethi, D. Nalianda, Y.-G. Li, L. Wang, Review of modern low emissions combustion technologies for aero gas turbine engines, Prog. Aerosp. Sci. 94 (2017) 12–45.
[2] M.M. Jaafar, K. Jusoff, M.S. Osman, M.S.A. Ishak, Combustor aerodynamic using radial swirler, Int. J. Phys. Sci. 6 (13) (2011) 3091–3098.
[3] W.A. Chishty, S.D. Lepera, U. Vandsburger, Spray combustion dynamics under thermoacoustic oscillations, Int. J. Mech. Mechatron. Eng. 5 (1) (2011) 234–239.
[4] T. Poinsot, D. Veynante, Theoretical and numerical combustion, RT Edwards, Inc., 2005.
[5] E. Riber, M. Moreau, O. Simonin, B. Cuenot, Development of Euler-Euler LES approach for gas-particle turbulent jet flow, in: Fluids Engineering Division Summer Meeting, vol. 47500, 2006, pp. 1663–1672.
[6] W. Jones, A. Marquis, K. Vogiatzaki, Large-eddy simulation of spray combustion in a gas turbine combustor, Combust. Flame 161 (1) (2014) 222–239.
[7] C. Mehl, S. Liu, Y.C. See, O. Colin, Les of a stratified turbulent burner with a thickened flame model coupled to adaptive mesh refinement and detailed chemistry, in: 2018 Joint Propulsion Conference, 2018, p. 4563.
[8] P. Wang, J. Fröhlich, U. Maas, Impact of location and flow rate oscillation of the pilot jet on the flow structures in swirling premixed flames, J. Turbul. 11 (2010) N11.
[9] J.-P. Legier, T. Poinsot, D. Veynante, Dynamically thickened flame les model for premixed and non-premixed turbulent combustion, Proceedings of the summer program, vol. 12, Citeseer, 2000, pp. 157–168.
[10] C. Huang, R. Gejji, W. Anderson, C. Yoon, V. Sankaran, Combustion dynamics in a single-element lean direct injection gas turbine combustor, Combust. Sci. Technol. 192 (12) (2020) 2371–2398.
[11] Y. Huang, S. Wang, V. Yang, Systematic analysis of lean-premixed swirl-stabilized combustion, AIAA J. 44 (4) (2006) 724–740.
[12] T. Poinsot, Prediction and control of combustion instabilities in real engines, Proc. Combust. Inst. 36 (1) (2017) 1–28.
[13] C. Huang, W.E. Anderson, M.E. Harvazinski, V. Sankaran, Analysis of self-excited combustion instabilities using decomposition techniques, AIAA J. 54 (9) (2016) 2791–2807.
[14] L. Selle, L. Benoit, T. Poinsot, F. Nicoud, W. Krebs, Joint use of compressible large-eddy simulation and helmholtz solvers for the analysis of rotating modes in an industrial swirled burner, Combust. Flame 145 (1–2) (2006) 194–205.
[15] F. Nicoud, L. Benoit, C. Sensiau, T. Poinsot, Acoustic modes in combustors with complex impedances and multidimensional active flames, AIAA J. 45 (2) (2007) 426–441.
[16] N. Syred, A review of oscillation mechanisms and the role of the precessing vortex core (pvc) in swirl combustion systems, Prog. Energy Combust. Sci. 32 (2) (2006) 93–161.
[17] J.M. Santiago, A. Verdier, G. Godard, A. Vandel, G. Cabot, M. Boukhalfa, B. Renou, Experimental study of airflow velocity, fuel droplet size-velocity and flame structure in a confined swirled jet-spray flame, in: ILASS–Europe 2016, 2016, F. Saint Etienne du Rouvray.
[18] J.M. Santiago, A. Verdier, C. Brunet, A. Vandel, G. Godard, G. Cabot, M. Boukhalfa, B. Renou, Experimental study of aeronautical ignition in a swirled confined jet-spray burner, in: Proceedings of the ASME turbo expo: Turbine technical conference and exposition, 2017.
[19] J. Marrero-Santiago, F. Collin-Bastiani, E. Riber, G. Cabot, B. Cuenot, B. Renou, On the mechanisms of flame kernel extinction or survival during aeronautical ignition sequences: Experimental and numerical analysis, Combust. Flame 222 (2020) 70–84.
[20] F. Collin-Bastiani, J. Marrero-Santiago, E. Riber, G. Cabot, B. Renou, B. Cuenot, A joint experimental and numerical study of ignition in a spray burner, Proc. Combust. Inst. 37 (4) (2019) 5047–5055.
[21] A. Broatch, M. Carreres, J. García-Tíscar, M. Belmar-Gil, Spectral analysis and modelling of the spray liquid injection in a lean direct injection (ldi) gas turbine combustor through Eulerian-Lagrangian large eddy simulations, Aerosp. Sci. Technol. 118 (2021) 106992.
[22] M. Belmar Gil, Computational study on the non-reacting flow in lean direct injection gas turbine combustors through Eulerian-Lagrangian large-eddy simulations, Doctoral Thesis, Universitat Politècnica de València, Mar. 2020.
[23] P. Senecal, E. Pomraning, K. Richards, T. Briggs, C. Choi, R. McDavid, M. Patterson, Multi-dimensional modeling of direct-injection diesel spray liquid length and flame lift-off length using cfd and parallel detailed chemistry, SAE Transact. (2003) 1331–1351.
[24] S.R. Turns, et al., Introduction to combustion, vol. 287, McGraw-Hill Companies, New York, NY, USA, 1996.
[25] C. Pichler, E. Nilsson, Analysis of important chemical pathways of n-heptane combustion in small skeletal mechanisms, Energy Fuels 34 (1) (2019) 758–768.
[26] J. Smagorinsky, General circulation experiments with the primitive equations: I. the basic experiment, Mon. Weather Rev. 91 (3) (1963) 99–164.
[27] R. Payri, R. Novella, M. Carreres, M. Belmar-Gil, Modeling gaseous non-reactive flow in a lean direct injection gas turbine combustor through an advanced mesh control strategy, Proceedings of the Institution of Mechanical Engineers, G, J. Aerosp. Eng. 234 (11) (2020) 1788–1810.
[28] P.J. O'Rourke, A.A. Amsden, The tab method for numerical calculation of spray droplet breakup, Tech. rep, Los Alamos National Lab, NM (USA), 1987.
[29] H. Werner, H. Wengle, Large-eddy simulation of turbulent flow over and around a cube in a plate channel, in: Turbulent shear flows 8, Springer, 1993, pp. 155–168.
[30] R.I. Issa, Solution of the implicitly discretised fluid flow equations by operator-splitting, J. Comput. Phys. 62 (1) (1986) 40–65.
[31] M. Carreres, L. García-Cuevas, J. García-Tíscar, M. Belmar-Gil, Spectral analysis of an aeronautical lean direct injection burner through large eddy simulation, Turbo Expo: Power for Land, Sea, and Air, vol. 84089, American Society of Mechanical Engineers, 2020, p. V02CT35A027.
[32] K. Taira, S.L. Brunton, S.T. Dawson, C.W. Rowley, T. Colonius, B.J. McKeon, O.T. Schmidt, S. Gordeyev, V. Theofilis, L.S. Ukeiley, Modal analysis of fluid flows: An overview, AIAA J. 55 (12) (2017) 4013–4041.
[33] A. Towne, O.T. Schmidt, T. Colonius, Spectral proper orthogonal decomposition and its relationship to dynamic mode decomposition and resolvent analysis, J. Fluid Mech. 847 (2018) 821–867.
[34] K. Taira, M.S. Hemati, S.L. Brunton, Y. Sun, K. Duraisamy, S. Bagheri, S.T. Dawson, C.-A. Yeh, Modal analysis of fluid flows: Applications and outlook, AIAA J. 58 (3) (2020) 998–1022.

[35] P.J. Schmid, Dynamic mode decomposition of numerical and experimental data, J. Fluid Mech. 656 (2010) 5–28.
[36] R. Futrzynski, G. Efraimsson, Dymode: A parallel dynamic mode decomposition software, 2015.
[37] J. Kou, W. Zhang, An improved criterion to select dominant modes from dynamic mode decomposition, Eur. J. Mech. B, Fluids 62 (2017) 109–129.
[38] S.B. Pope, Ten questions concerning the large-eddy simulation of turbulent flows, New J. Phys. 6 (1) (2004) 35.
[39] F. Shum-Kivan, Simulation des grandes echelles de flammes de spray et modélisation de la combustion non-prémélangée, Ph.D. thesis, 2017.
[40] F. Collin-Bastiani, Modeling and numerical simulations of two-phase ignition in gas turbine, PhD, Institut National Polytechnique de Toulouse, 2019.
[41] P. Agostinelli, D. Laera, I. Boxx, L. Gicquel, T. Poinsot, Impact of wall heat transfer in large eddy simulation of flame dynamics in a swirled combustion chamber, Combust. Flame 234 (2021) 111728.
[42] C.F. Silva, M. Leyko, F. Nicoud, S. Moreau, Assessment of combustion noise in a premixed swirled combustor via large-eddy simulation, Comput. Fluids 78 (2013) 1–9.
[43] J. Weiss, A tutorial on the proper orthogonal decomposition, in: AIAA aviation 2019 forum, 2019, p. 3333.
[44] K. Oberleithner, M. Sieber, C.N. Nayeri, C.O. Paschereit, C. Petz, H.-C. Hege, B.R. Noack, I. Wygnanski, Three-dimensional coherent structures in a swirling jet undergoing vortex breakdown: stability analysis and empirical mode construction, J. Fluid Mech. 679 (2011) 383–414.
[45] G. Vignat, D. Durox, K. Prieur, S. Candel, An experimental study into the effect of injector pressure loss on self-sustained combustion instabilities in a swirled spray burner, Proc. Combust. Inst. 37 (4) (2019) 5205–5213.